IEEE Access
Multidisciplinary | Rapid Review | Open Access Journal

Received May 10, 2019, accepted May 24, 2019, date of publication May 28, 2019, date of current version June 7, 2019.

Digital Object Identifier 10.1109/ACCESS.2019.2919670

Velocity-Free Saturated Control for Hovering Over an Asteroid With Disturbance Rejection

BO ZHANG AND YUANLI CAI
Department of Automation Science and Technology, Xi'an Jiaotong University, Xi'an 710049, China
Corresponding author: Yuanli Cai (ylicai@mail.xjtu.edu.cn)

This work was supported in part by the China Postdoctoral Science Foundation under Grant 2018M640995.

ABSTRACT Hovering over an asteroid is challenging due to both the large gravitational uncertainty and the strong external disturbance. When a spacecraft is not equipped with velocity sensors to simplify the navigation system and reduce the mass and costs, or the velocity sensors malfunction, the situation may be worse. In this paper, an extended state observer (ESO) is devised to estimate the velocity and the lumped disturbance simultaneously. The estimate errors are proved to be uniformly ultimately bounded with the assumption that the change rate of the lumped disturbance is bounded. To cope with control input saturation, a backstepping controller in conjunction with an auxiliary system is proposed for the hovering. Combining the controller with the ESO, we develop a disturbance rejection control scheme without velocity feedback. The stability of the whole closed-loop system is analyzed via the Lyapunov theory, showing that the control scheme can drive a spacecraft to the neighborhood of the desired hovering state. The numerical simulations of both body-fixed hovering and inertial hovering are conducted to demonstrate the effectiveness of the proposed scheme.

INDEX TERMS Asteroid hovering, backstepping control, extended state observer, input saturation.

I. INTRODUCTION

Recent years, the research on asteroids has gained increasing interest for the purposes of science exploration, hazard prevention and resource identification [1]. In asteroid exploration missions, hovering plays a key role in asteroid surface mapping, landing site candidate identification, lander deployment, etc. In addition, hovering is much easier than designing a stable orbit around the small body in the extremely irregular gravitational filed. In the Hayabusa mission of the Japanese Aerospace Exploration Agency (JAXA), a hovering approach was applied to the spacecraft for scientific observation of asteroid 25143 Itokawa [2].

However, hovering over an asteroid is rather challenging in that the extremely irregular shape of a small body results in large gravitational uncertainties, and the weak gravity is prone to be disturbed by solar radiation pressure and gravitational attraction of other celestial bodies. What is worse, the dynamic environment, the shape, and the rotational state of an asteroid are hard to be known through remote observation. In asteroid exploration missions, the control authority of the spacecraft is usually quite limited, and thereby control input saturation is another problem should be taken into account. Due to the challenges of the hovering, plenty of research has been devoted to designing control schemes for asteroid hovering spacecrafts. Sawai and Scheeres [3] characterized the ability of hovering control with only one-dimensional altimetry measurements by linearizing the equations of motion, and some ideal control methodologies yielding stable hovering trajectories were found. However, in this study, the assumption of infinitely tight control is not realistic. Hence, the previous work was furthered to investigate the stability of hovering under dead-band control of the altitude by numerically simulating the nonlinear equations of motion [4]. Then, the dead-band control methodology was applied to time-invariant Lagrangian dynamical systems and the sufficient conditions for local and global boundedness were derived [5]. To eliminate the requirement of a priori knowledge of the environment in asteroids' vicinity, Gaudet and Furfaro [6] employed reinforcement learning to develop a hovering controller with sufficient robustness to allow precise hovering in unknown environments. For a tumbling asteroid, Nazari *et al.* [7] studied body-frame hovering by using time-varying LQR and the combination of Lyapunov-Floquet transformation and time-invariant LQR, with the state vectors estimated by an observer. However, the observer cannot

The associate editor coordinating the review of this manuscript and approving it for publication was Qilian Liang.

estimate disturbances to improve hovering accuracy. In order to reject disturbances, Furfaro [8] devised a class of discontinuous two-sliding homogeneous controllers for hovering by employing the higher-order sliding mode theory. Zeng *et al.* [9] investigated body-fixed hovering of the spacecraft equipped with compact form of controllable nonideal solar sails, and then body-fixed hovering flight over an elongated asteroid using solar sail technique was studied with the asteroid taken as a rotating mass dipole [10]. Employing the sliding mode control theory, Lee *et al.* [11]–[13] developed a series of controllers for asteroid hovering in the framework of geometric mechanics, which stabilized the orbit and the attitude of a spacecraft simultaneously. Using the non-canonical Hamiltonian structure in the body-fixed orbit-attitude hovering problem, Wang and Xu [14] proposed a feedback hovering control law for a rigid spacecraft. Liu *et al.* [15] designed a 6-DOF controller for a rigid spacecraft with control input saturation handled by a RBF network. Gui and Ruiter [16] designed an ESO to estimate the spacecraft velocity and the disturbance simultaneously, based on which a disturbance rejection PD-like hovering control scheme was developed without velocity feedback. By using the terminal sliding mode control theory, Yang *et al.* [17] designed a finite-time controller for asteroid hovering and landing in the presence of uncertainties and disturbances in the vicinity of asteroids. In [1], a controller with both control input saturation and its change rate saturation considered was developed for asteroid hovering by full use of the sliding mode theory. Zhang and Cai [18] developed an adaptive controller for the spacecraft hovering over an asteroid with unknown parameters. The control scheme deals with unknown parameters well, but it is hard to estimate uncertainties and disturbances in the design.

In general, the position and velocity of a spacecraft are required to design a controller for hovering over an asteroid to achieve appropriate transient process and high final accuracy. However, velocity sensors may be too cumbersome for the spacecraft to investigate an asteroid. Using only position measurement to implement hovering [3]–[5], [16] implies the potential benefit of simplifying the navigation system and reducing the mass and costs of a spacecraft. Besides, a velocity-free controller is vital to the success of a mission when onboard velocity sensors malfunction. However, in the absence of velocity feedback, a controller is hard to achieve desired performance due to lack of damping. In addition, large uncertainties and strong disturbances in the vicinity of asteroids also corrupt the controller of a hovering spacecraft every moment. Recently, the controller for spacecrafts and aircrafts with disturbances explicitly rejected were widely studied to improve robustness [16], [19]–[26]. However, it is obvious that a disturbance observer [19], [20] is not adequate for our controller design because the velocity needs to be estimated as well. Therefore, an ESO is pivotal to the hovering controller without velocity measurement, owing to its capability of estimating the velocity and disturbance simultaneously. First devised by Han [27], an ESO is a high gain state observer that regards the lumped uncertainty as an augmented state, which has be widely used to design controllers for spacecrafts and aircrafts. Yang *et al.* [21] applied an ESO to the problem of attitude synchronization of spacecraft formation. Zarovy and Costello [22] used an ESO to estimate the mass and center-of-gravity location of a helicopter online, and the estimate accuracy is demonstrated by Monte Carlo trade studies. A linear ESO was proposed in [28] by setting the parameters of Han's ESO to some special values, which was used to robustify an input-output linearization based controller for wing rock motion. A novel ESO for a class of nonlinear systems subject to multiple uncertainties was presented in [23], and then it was applied to partial integrated guidance and control design for missiles. Li *et al.* [24] combined an ESO with an inverse optimal controller to stabilize the attitude of a spacecraft with input saturation. Shao *et al.* [29] developed a high-order ESO by following the principle of high-gain observer design, and applied it to a trajectory tracking controller for quadrotors.

In this paper, a novel controller for accurate asteroid hovering is developed with only the position of the spacecraft used. To estimate the velocity of the spacecraft and the lumped disturbance in the vicinity of an asteroid, an ESO is devised to ensure the estimate errors are ultimately bounded. Then a backstepping controller in conjunction with an auxiliary system is developed to stabilize the trajectory of the spacecraft to the desired hovering state in the presence of control input saturation. For the sake of disturbance rejection, the estimated disturbance is introduced to the controller to counteract the real total disturbance. Meanwhile, the velocity in the controller is replaced by the estimated velocity to realize a velocity-free controller.

The rest of this paper is organized as follows. In Section II, the equations of motion for the spacecraft is described in a body-fixed coordinate frame and the asteroid hovering problem is formulated. Then, in Section III, a novel ESO is proposed and the dynamics of the estimate errors is established, and the ultimate boundedness of the estimate errors is proved via Lyapunov theory. The backstepping control scheme for asteroid hovering with input saturation considered is devised in Section IV, which is combined with the proposed ESO to accomplish the disturbance rejection velocity-free controller; after that the stability of the entire closed-loop system is proved. Numerical simulations are conducted in Section V to demonstrate the effectiveness of the proposed method. Finally, some conclusions are drawn in Section VI.

II. PROBLEM FORMULATION

The body-fixed and inertial hovering problems are both considered in this paper. Hence, it is necessary to introduce the body-fixed and inertial reference frames to describe the proximity operations. As shown in Fig. 1, the origin of the body-fixed frame $o-xyz$ is located at the mass center of the asteroid, the z-axis aligned with the rotation angular velocity $\boldsymbol{\omega}$. The x-axis and y-axis coincide with the axes of the minimum and middle moment of inertia to complete a right-handed coordinate frame. The body-fixed frame shares

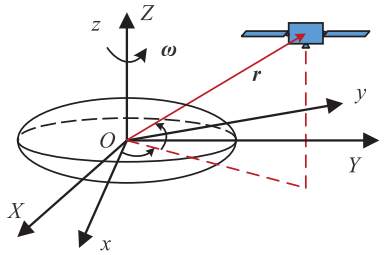

FIGURE 1. Definition of the coordinate frames [1].

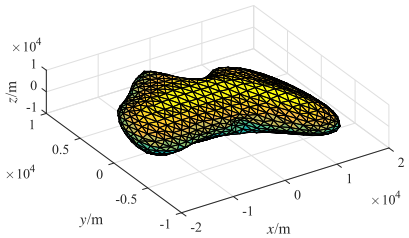

FIGURE 2. Polyhedron shape model of asteroid 433 Eros [1].

its origin with the inertial frame, and the three axes of the inertial frame are fixed in inertial space and coincident with those of the body fixed frame in time zero. Coordinate transforming from the inertial frame to the body-fixed frame is achieved by virtue of the following transformation matrix [1]:

$$T(\omega t) = \begin{bmatrix} \cos(\omega t) & \sin(\omega t) & 0 \\ -\sin(\omega t) & \cos(\omega t) & 0 \\ 0 & 0 & 1 \end{bmatrix},$$

where ω is the magnitude of $\boldsymbol{\omega}$, and t represents time.

In the formulation of the hovering problem, a two-body gravity model is used as the mass of the spacecraft is negligible compared with that of the small body. For the convenience of computing the gravitational acceleration vector, the dynamics of the spacecraft in the vicinity of an asteroid is established in the body-fixed frame in this paper [3], [7], [8], [17], which is described by

$$\dot{\boldsymbol{r}} = \boldsymbol{v}, \tag{1}$$

$$\dot{\boldsymbol{v}} = -2\boldsymbol{\omega} \times \boldsymbol{v} - \boldsymbol{\omega} \times (\boldsymbol{\omega} \times \boldsymbol{r}) + \boldsymbol{g}(\boldsymbol{r}) + \boldsymbol{a}_c + \boldsymbol{d}, \tag{2}$$

where $\boldsymbol{r} \in \mathbb{R}^3$ is the position vector, $\boldsymbol{v} \in \mathbb{R}^3$ the velocity vector; $\boldsymbol{\omega} = [0, 0, \omega]^{\mathrm{T}}$ is the angular velocity of the asteroid; $\boldsymbol{a}_c \in \mathbb{R}^3$ is the control acceleration provided by the thrusters; $\boldsymbol{g}(\boldsymbol{r}) \in \mathbb{R}^3$ is the acceleration due to the gravity of the asteroid; $\boldsymbol{d} \in \mathbb{R}^3$ is the lumped disturbance, which can be expressed as

$$\boldsymbol{d} = \boldsymbol{a}_{\mathrm{spr}} + \boldsymbol{a}_{\mathrm{other}} + \Delta\boldsymbol{g},$$

where $\boldsymbol{a}_{\mathrm{spr}}$ is the solar pressure acceleration, $\boldsymbol{a}_{\mathrm{other}}$ the gravitational acceleration caused by other celestial bodies, and $\Delta\boldsymbol{g}$ the uncertainty of $\boldsymbol{g}(\boldsymbol{r})$. The effect of these quantities is relatively significant, but they cannot be accurately measured or calculated, thereby considered as disturbances [8], [17].

The gravitational acceleration can be expressed as

$$\boldsymbol{g}(\boldsymbol{r}) = \frac{\partial U}{\partial \boldsymbol{r}},$$

where U is the potential function of the gravitational field. Because the shape of an asteroid is very irregular (the polyhedron shape model of asteroid 433 Eros is shown in Fig. 2 as an example), U is usually obtained via the spherical harmonics expansion or the polyhedron gravity model. When a spacecraft flies near an asteroid, the position of the spacecraft may be inside the Brillouin sphere where the spherical harmonics gravity model is no longer guaranteed to converge [30]. Therefore, the polyhedron gravity model [30] is employed in this paper:

$$U = \frac{1}{2} G\rho \sum_{e \in \mathrm{edges}} L_e \boldsymbol{r}_e^{\mathrm{T}} \boldsymbol{E}_e \boldsymbol{r}_e - \frac{1}{2} G\rho \sum_{f \in \mathrm{faces}} \omega_f \boldsymbol{r}_f^{\mathrm{T}} \boldsymbol{F}_f \boldsymbol{r}_f$$

$$\frac{\partial U}{\partial \boldsymbol{r}} = -G\rho \sum_{e \in \mathrm{edges}} L_e \boldsymbol{E}_e \boldsymbol{r}_e + G\rho \sum_{f \in \mathrm{faces}} \omega_f \boldsymbol{F}_f \boldsymbol{r}_f$$

where G is the gravitational constant, ρ represents the bulk density of an asteroid, and the other symbols and more details of the polyhedron gravity model can be found in [30].

To take the control input saturation into consideration, the commanded acceleration is restricted by

$$\boldsymbol{a}_c = \mathrm{sat}(\boldsymbol{u}) = \begin{bmatrix} \mathrm{sat}(u_x) \\ \mathrm{sat}(u_y) \\ \mathrm{sat}(u_z) \end{bmatrix}, \quad \boldsymbol{u} = \begin{bmatrix} u_x \\ u_y \\ u_z \end{bmatrix} \in \mathbb{R}^3,$$

where sat is defined as

$$\mathrm{sat}(u_i) = \begin{cases} u_{\max}, & u_i > u_{\max} \\ u_i, & -u_{\max} \le u_i \le u_{\max} \\ -u_{\max}, & u_i < -u_{\max} \end{cases}, \quad i = x, y, z,$$

where $u_{\max}$ is the maximum control authority in each direction that can be provided by the thrusters.

Now, the goal of the hovering control can be addressed as steering the spacecraft to the desired location $\boldsymbol{r}_d$ and afterwards maintaining the hovering in the vicinity of the asteroid, with the commanded acceleration $\boldsymbol{a}_c$ bounded by $\|\boldsymbol{a}_c\|_\infty \le u_{\max}$, despite the presence of the disturbance $\boldsymbol{d}$.

III. EXTENDED STATE OBSERVER

In the scenarios studied in this paper, the velocity of the spacecraft $\boldsymbol{v}$ and the disturbance $\boldsymbol{d}$ are unknown. To estimate the velocity and the total disturbance from the position vector $\boldsymbol{r}$, an ESO is designed in this section. The ESO regards the disturbance as an extended state of the system and estimates it together with the unattainable state $\boldsymbol{v}$. Denote the estimates of $\boldsymbol{v}$ and $\boldsymbol{d}$ by $\hat{\boldsymbol{v}}$ and $\hat{\boldsymbol{d}}$ respectively, and then the ESO is formulated as

$$\dot{\boldsymbol{\chi}} = \boldsymbol{\beta} + \kappa_1 \boldsymbol{r}, \tag{3}$$

$$\dot{\boldsymbol{\beta}} = -2\boldsymbol{\omega} \times \hat{\boldsymbol{v}} - \boldsymbol{\omega} \times (\boldsymbol{\omega} \times \boldsymbol{r}) + \boldsymbol{g}(\boldsymbol{r}) + \boldsymbol{a}_c + \hat{\boldsymbol{d}} - \kappa_1 (\boldsymbol{\beta} + \kappa_1 \boldsymbol{r}) + \kappa_2 \boldsymbol{\zeta}, \tag{4}$$

$$\dot{\hat{\boldsymbol{d}}} = \kappa_3 \boldsymbol{\zeta}, \tag{5}$$

where

$$\boldsymbol{\zeta} = \boldsymbol{r} - \boldsymbol{\chi}, \tag{6}$$

and $\kappa_1, \kappa_2 > 0$ are observer gains; $\boldsymbol{\chi}$, $\boldsymbol{\beta}$ and $\hat{\boldsymbol{d}}$ are the states of the ESO. The outputs of the ESO are

$$\hat{\boldsymbol{v}} = \boldsymbol{\beta} + \kappa_1 \boldsymbol{r}, \tag{7}$$

$$\hat{\boldsymbol{d}} = \kappa_3 \int_0^t \boldsymbol{\zeta}(\tau)\, \mathrm{d}\tau, \tag{8}$$

In this paper, the term $\hat{\boldsymbol{d}}$ not only contains the uncertainty of asteroid's gravity, but also comprises other disturbances. Therefore, $\hat{\boldsymbol{d}}$ is more helpful to the controller than the estimates of the gravity model parameters [7], [11], [18].

To begin the analysis of the ESO's stability, the estimate errors are defined as

$$\tilde{\boldsymbol{v}} = \boldsymbol{v} - \hat{\boldsymbol{v}}, \tag{9}$$

$$\tilde{\boldsymbol{d}} = \boldsymbol{d} - \hat{\boldsymbol{d}}. \tag{10}$$

Differentiating (9) and (10) yields

$$\dot{\tilde{\boldsymbol{v}}} = -2\boldsymbol{\omega} \times \tilde{\boldsymbol{v}} - \kappa_1 \tilde{\boldsymbol{v}} - \kappa_2 \boldsymbol{\zeta} + \tilde{\boldsymbol{d}}, \tag{11}$$

$$\dot{\tilde{\boldsymbol{d}}} = -\kappa_3 \boldsymbol{\zeta} + \dot{\boldsymbol{d}}. \tag{12}$$

From (3), (6) and (7), the dynamics of $\boldsymbol{\zeta}$ can be obtained:

$$\dot{\boldsymbol{\zeta}} = \tilde{\boldsymbol{v}}. \tag{13}$$

Thus, (11), (12), and (13) represent the dynamics of the estimate errors. Rewriting the equations of the dynamics in a compact form yields

$$\begin{bmatrix} \dot{\boldsymbol{\zeta}} \\ \dot{\tilde{\boldsymbol{v}}} \\ \dot{\tilde{\boldsymbol{d}}} \end{bmatrix} = \begin{bmatrix} 0_{3\times3} & I_3 & 0_{3\times3} \\ -\kappa_2 I_3 & -\kappa_1 I_3 - 2\boldsymbol{\omega}^{\times} & I_3 \\ -\kappa_3 I_3 & 0_{3\times3} & 0_{3\times3} \end{bmatrix} \begin{bmatrix} \boldsymbol{\zeta} \\ \tilde{\boldsymbol{v}} \\ \tilde{\boldsymbol{d}} \end{bmatrix} + \begin{bmatrix} 0 \\ 0 \\ \dot{\boldsymbol{d}} \end{bmatrix}, \tag{14}$$

where I_3 is the 3×3 identity matrix, and $0_{3\times3}$ represents the 3×3 zero matrix. $\boldsymbol{\omega}^{\times}$ is a skew-symmetric matrix given by

$$\boldsymbol{\omega}^{\times} = \begin{bmatrix} 0 & -\omega & 0 \\ \omega & 0 & 0 \\ 0 & 0 & 0 \end{bmatrix}.$$

For convenience, the following variables are defined:

$$\boldsymbol{\vartheta}_1 = \frac{\boldsymbol{\zeta}}{\varepsilon^2}, \quad \boldsymbol{\vartheta}_2 = \frac{\tilde{\boldsymbol{v}}}{\varepsilon}, \quad \boldsymbol{\vartheta}_3 = \tilde{\boldsymbol{d}}, \tag{15}$$

$$\kappa_1 = \frac{h_1}{\varepsilon}, \quad \kappa_2 = \frac{h_2}{\varepsilon^2}, \quad \kappa_3 = \frac{h_3}{\varepsilon^3}. \tag{16}$$

where ε is a small positive constant. Then, (14) can be written as

$$\dot{\boldsymbol{\vartheta}} = \varepsilon^{-1} A \boldsymbol{\vartheta} + \boldsymbol{p}, \tag{17}$$

where

$$\boldsymbol{\vartheta} = \begin{bmatrix} \boldsymbol{\vartheta}_1 \\ \boldsymbol{\vartheta}_2 \\ \boldsymbol{\vartheta}_3 \end{bmatrix}, \quad \boldsymbol{p} = \begin{bmatrix} 0_{1\times3} \\ 0_{1\times3} \\ \dot{\boldsymbol{d}} \end{bmatrix},$$

$$A = \begin{bmatrix} 0_{3\times3} & I_3 & 0_{3\times3} \\ -h_2 I_3 & -h_1 I_3 - 2\varepsilon\boldsymbol{\omega}^{\times} & I_3 \\ -h_3 I_3 & 0_{3\times3} & 0_{3\times3} \end{bmatrix}.$$

Assume $\dot{\boldsymbol{d}}$ is bounded by $\| \dot{\boldsymbol{d}} \|_2 \leq \psi$. Then, it is obvious that the right-hand side of (17) consists of a linear part and a bounded unknown disturbance. To simplify the analysis of the perturbed system (17), the nominal system with vanishing perturbation is considered firstly [31]:

$$\dot{\boldsymbol{\vartheta}} = \varepsilon^{-1} A \boldsymbol{\vartheta}.$$

The characteristic polynomial of A is

$$p(s) = \det(sI_9 - A) = -p_1(s)\, p_2(s),$$

where

$$\begin{aligned} p_1(s) &= s^3 + h_1 s^2 + h_2 s + h_3, \\ p_2(s) &= s^6 + 2h_1 s^5 + \left(h_1^2 + 2h_2 + 4\varepsilon^2\omega^2\right) s^4 \\ &\quad + (2h_1 h_2 + 2h_3)\, s^3 + \left(2h_1 h_3 + h_2^2\right) s^2 \\ &\quad + 2h_2 h_3 s + h_3^2. \end{aligned}$$

Evidently, $p(s)$ is Hurwitz if and only if both $p_1(s)$ and $p_2(s)$ are Hurwitz. In accordance with Routh-Hurwitz criterion, $p_1(s)$ is Hurwitz if

$$\begin{vmatrix} h_1 & h_3 & 0 \\ 1 & h_2 & 0 \\ 0 & h_1 & h_3 \end{vmatrix} > 0, \quad \begin{vmatrix} h_1 & h_3 \\ 1 & h_2 \end{vmatrix} > 0, \; h_1 > 0. \tag{18}$$

Solving the inequalities in (18), we get

$$h_1 > 0, \quad h_3 > 0, \; h_2 > \frac{h_3}{h_1}. \tag{19}$$

From the results in (19), it is readily to conclude that the coefficients of the polynomial $p_2(s)$ are all positive. Therefore, $p_2(s)$ is Hurwitz if the following conditions hold:

$$2h_1 > 0, \quad \det(H_{3\times3}) > 0, \; \det\begin{bmatrix} H_{3\times3} & H_{3\times2} \\ H_{2\times3} & H_{2\times2} \end{bmatrix} > 0,$$

where

$$H_{3\times3} = \begin{bmatrix} 2h_1 & 2h_1 h_2 + 2h_3 & 2h_2 h_3 \\ 1 & h_1^2 + 2h_2 + 4\varepsilon^2\omega^2 & 2h_1 h_3 + h_2^2 \\ 0 & 2h_1 & 2h_1 h_2 + 2h_3 \end{bmatrix},$$

$$H_{3\times2} = \begin{bmatrix} 0 & 0 \\ h_3^2 & 0 \\ 2h_2 h_3 & 0 \end{bmatrix},$$

$$H_{2\times3} = \begin{bmatrix} 0 & 1 & h_1^2 + 2h_2 + 4\varepsilon^2\omega^2 \\ 0 & 0 & 2h_1 \end{bmatrix},$$

$$H_{2\times2} = \begin{bmatrix} 2h_1 h_3 + h_2^2 & h_3^2 \\ 2h_1 h_2 + 2h_3 & 2h_2 h_3 \end{bmatrix}.$$

With tedious but straightforward algebraic operations, the following inequalities are achieved:

$$h_1 > 0, \tag{20}$$

$$h_1^4 h_2 - h_1^3 h_3 + h_1 h_2 h_3 - h_3^2 + 4\left(h_1^2 h_2 + h_1 h_3\right)\varepsilon^2\omega^2 > 0, \tag{21}$$

$$h_3\left(h_1^2h_2^2-2h_1h_2h_3+h_3^2+4h_2^2\varepsilon^2\omega^2\right)\times\left(h_1^2h_2^2-2h_1h_2h_3+h_3^2-4h_1h_3\varepsilon^2\omega^2\right)>0. \quad (22)$$

Solving (20)-(22) in conjunction with (19), one obtains

$$h_1>0,\quad h_3>0,\ h_2>\frac{h_3}{h_1}+2\varepsilon\omega\sqrt{\frac{h_3}{h_1}}. \quad (23)$$

Hence, if h_1, h_2 and h_3 satisfy the conditions in (23), matrix A is Hurwitz. In accordance with Lyapunov stability theorem of linear systems, there exist symmetric positive definite matrices P and Q satisfying Lyapunov equation [31]

$$PA+A^{\mathrm{T}}P=-Q. \quad (24)$$

In order to analyze the stability of the perturbed system (17), Lyapunov function candidate (25) is selected:

$$V_\vartheta=\boldsymbol{\vartheta}^{\mathrm{T}}P\boldsymbol{\vartheta}. \quad (25)$$

Thus, we have

$$\lambda_{\min}(P)\parallel\boldsymbol{\vartheta}\parallel_2^2\le V_\vartheta\le\lambda_{\max}(P)\parallel\boldsymbol{\vartheta}\parallel_2^2, \quad (26)$$

where $\lambda_{\min}(P)$ and $\lambda_{\max}(P)$ are the minimum and the maximum eigenvalues of P respectively. Differentiating (25) leads to

$$\begin{aligned}\dot V_\vartheta&=\boldsymbol{\vartheta}^{\mathrm{T}}P\dot{\boldsymbol{\vartheta}}+\dot{\boldsymbol{\vartheta}}^{\mathrm{T}}P\boldsymbol{\vartheta}\\&=\boldsymbol{\vartheta}^{\mathrm{T}}P\left(\varepsilon^{-1}A\boldsymbol{\vartheta}+\boldsymbol{p}\right)+\left(\varepsilon^{-1}A\boldsymbol{\vartheta}+\boldsymbol{p}\right)^{\mathrm{T}}P\boldsymbol{\vartheta}\\&\le-\varepsilon^{-1}\boldsymbol{\vartheta}^{\mathrm{T}}Q\boldsymbol{\vartheta}+2\boldsymbol{\vartheta}^{\mathrm{T}}P\boldsymbol{p}\\&\le-\varepsilon^{-1}\lambda_{\min}(Q)\parallel\boldsymbol{\vartheta}\parallel_2^2+2\lambda_{\max}(P)\psi\parallel\boldsymbol{\vartheta}\parallel_2\\&\le-\varepsilon^{-1}\frac{\lambda_{\min}(Q)}{\lambda_{\max}(P)}V_\vartheta+2\psi\frac{\lambda_{\max}(P)}{\sqrt{\lambda_{\min}(P)}}\sqrt{V_\vartheta}.\end{aligned}$$

To obtain a linear differential inequality that is easy to tackle, we take $W_\vartheta(t)=\sqrt{V_\vartheta}$ and invoke the fact that $\dot W_\vartheta=\dot V_\vartheta/\left(2\sqrt{V_\vartheta}\right)$. Thus, when $V_\vartheta\neq0$, we have

$$\dot W_\vartheta\le-\frac{1}{2}\varepsilon^{-1}\frac{\lambda_{\min}(Q)}{\lambda_{\max}(P)}W_\vartheta+\psi\frac{\lambda_{\max}(P)}{\sqrt{\lambda_{\min}(P)}}. \quad (27)$$

By the comparison principle [31], the following inequality is derived from (27)

$$W_\vartheta\le[W(0)-C_0]\exp\left[-\frac{1}{2\varepsilon}\frac{\lambda_{\min}(Q)}{\lambda_{\max}(P)}t\right]+C_0,$$

where

$$C_0=\frac{2\varepsilon\psi\lambda_{\max}^2(P)}{\lambda_{\min}(Q)\sqrt{\lambda_{\min}(P)}}.$$

Invoking (26), one gets the upper bound of $\parallel\boldsymbol{\vartheta}\parallel_2$ immediately:

$$\parallel\boldsymbol{\vartheta}\parallel_2\le\frac{\sqrt{V_\vartheta(0)}-C_0}{\sqrt{\lambda_{\min}(P)}}\exp\left[-\frac{1}{2\varepsilon}\frac{\lambda_{\min}(Q)}{\lambda_{\max}(P)}t\right]+\frac{C_0}{\sqrt{\lambda_{\min}(P)}}.$$

It is clearly that

$$\limsup_{t\to\infty}\parallel\boldsymbol{\vartheta}\parallel_2\le C=\frac{2\varepsilon\psi\lambda_{\max}^2(P)}{\lambda_{\min}(Q)\lambda_{\min}(P)}. \quad (28)$$

From the analysis, it can be concluded that $\boldsymbol{\vartheta}$ is uniformly ultimately bounded with the upper bound given by (28). Consequently, from (15), the ultimate upper bounds of the estimate errors are given by

$$\limsup_{t\to\infty}\parallel\boldsymbol{\zeta}\parallel_2\le\varepsilon^2C, \quad (29)$$

$$\limsup_{t\to\infty}\parallel\tilde{\boldsymbol{v}}\parallel_2\le\varepsilon C, \quad (30)$$

$$\limsup_{t\to\infty}\parallel\tilde{\boldsymbol{d}}\parallel_2\le C. \quad (31)$$

For a set of specified values of h_1, h_2 and h_3 that satisfy conditions in (23), as ε goes to zero, the stability of A is not influenced. Thereby there always exist symmetric positive definite matrices P and Q to meet Lyapunov equality (24) as $\varepsilon\to0$. This fact implies that

$$\lim_{\varepsilon\to0}\frac{\lambda_{\max}^2(P)}{\lambda_{\min}(Q)\lambda_{\min}(P)}=\delta_0\in\mathbb{R}^+.$$

Thus, we have $C\to0$, as $\varepsilon\to0$.

Remark 1: Equations (29) - (31) indicate that decreasing ε can improve the estimate accuracy of the ESO. However, when measurement uncertainties of $\boldsymbol{r}$ are present in the ESO, any tiny uncertainties will be amplified excessively if ε is too small, which is easy to be drawn from (15). Therefore, ε should be tuned to make a trade-off between the estimate accuracy and the robustness to uncertainties.

IV. SATURATED BACKSTEPPING CONTROLLER WITHOUT VELOCITY MEASUREMENT

As mentioned previously, spacecrafts for asteroid exploration missions are usually equipped with low thrust engines with large specific impulses to attain longer exploration time. On the other hand, the low thrust renders the controller prone to be saturated. To simplify the navigation system and reduce the mass and costs, a spacecraft without velocity sensors is preferred from a practical point of view. Additionally, when the velocity sensors of a spacecraft malfunction, a controller does not rely on velocity feedback is an essential alternative for the mission. In this section, base on the proposed ESO, a saturated controller for asteroid hovering without velocity measurement is derived. The stability of the closed-loop system is established via Lyapunov analysis in the presence of disturbances.

A. FULL STATE SATURATED BACKSTEPPING CONTROLLER DESIGN

First, according to the backstepping technique [31], [32], the position error is defined as

$$\boldsymbol{z}_1=\gamma_1(\boldsymbol{r}-\boldsymbol{r}_d), \quad (32)$$

where $\gamma_1>0$. Taking derivative of $\boldsymbol{z}_1$ gives

$$\dot{\boldsymbol{z}}_1=\gamma_1(\dot{\boldsymbol{r}}-\dot{\boldsymbol{r}}_d). \quad (33)$$

Select a candidate Lyapunov function as

$$V_1=\frac{1}{2}\boldsymbol{z}_1^{\mathrm{T}}\boldsymbol{z}_1. \quad (34)$$

Differentiating (34), one gets

$$\dot{V}_1 = z_1^{\mathrm{T}}\dot{z}_1 = \gamma_1 z_1^{\mathrm{T}}\left(\boldsymbol{v} - \dot{\boldsymbol{r}}_d\right). \tag{35}$$

To render the derivative of V_1 negative definite, the virtual control is given by

$$\boldsymbol{v}^0 = -k_1 z_1 + \dot{\boldsymbol{r}}_d, \tag{36}$$

where $k_1 > 0$. Then, define

$$z_2 = \boldsymbol{v} - \boldsymbol{v}^0 = \boldsymbol{v} + k_1 z_1 - \dot{\boldsymbol{r}}_d. \tag{37}$$

Substituting (36) and (32) into (33) and denoting the derivative of z_2 by $\boldsymbol{v}$, we have

$$\dot{z}_1 = -k_1\gamma_1 z_1 + \gamma_1 z_2, \tag{38}$$
$$\dot{z}_2 = \boldsymbol{v}. \tag{39}$$

Consider the following Lyapunov function candidate:

$$V_2 = V_1 + \frac{1}{2}\left(z_2 - \boldsymbol{\xi}\right)^{\mathrm{T}}\left(z_2 - \boldsymbol{\xi}\right) + \frac{1}{2}\boldsymbol{\xi}^{\mathrm{T}}\boldsymbol{\xi},$$

where $\boldsymbol{\xi}$ is an auxiliary variable whose dynamics will be designed later to cope with input saturation. The derivative of V_2 along the trajectory of (38) and (39) is

$$\begin{aligned}\dot{V}_2 &= \dot{V}_1 + \left(z_2 - \boldsymbol{\xi}\right)^{\mathrm{T}}\left(\dot{z}_2 - \dot{\boldsymbol{\xi}}\right) + \boldsymbol{\xi}^{\mathrm{T}}\dot{\boldsymbol{\xi}} \\ &= -k_1\gamma_1 z_1^{\mathrm{T}} z_1 + \gamma_1 z_1^{\mathrm{T}} z_2 + \left(z_2 - \boldsymbol{\xi}\right)^{\mathrm{T}}\left(\boldsymbol{v} - \dot{\boldsymbol{\xi}}\right) + \boldsymbol{\xi}^{\mathrm{T}}\dot{\boldsymbol{\xi}}.\end{aligned} \tag{40}$$

Application of Lyapunov stability theory to (40) yields the following results:

$$\boldsymbol{v} = -\gamma_1 z_1 - k_2\left(z_2 - \boldsymbol{\xi}\right) + \dot{\boldsymbol{\xi}}, \tag{41}$$
$$\dot{\boldsymbol{\xi}} = -k_3\boldsymbol{\xi} + \Delta\boldsymbol{u}, \tag{42}$$

where $k_2 > 0$, $k_3 > 0$ and $\Delta\boldsymbol{u} = \mathrm{sat}\left(\boldsymbol{u}\right) - \boldsymbol{u}$. Assume $\Delta\boldsymbol{u}$ is bounded by $\parallel \Delta\boldsymbol{u} \parallel_2 \leq \varphi$. Substituting (41) and (42) into (40), we get

$$\begin{aligned}\dot{V}_2 &= -\gamma_1\, k_1 z_1^{\mathrm{T}} z_1 - k_2\left(z_2 - \boldsymbol{\xi}\right)^{\mathrm{T}}\left(z_2 - \boldsymbol{\xi}\right) + \gamma_1\boldsymbol{\xi}^{\mathrm{T}} z_1 \\ &\quad - k_3\boldsymbol{\xi}^{\mathrm{T}}\boldsymbol{\xi} + \boldsymbol{\xi}^{\mathrm{T}}\Delta\boldsymbol{u} \\ &= \boldsymbol{\xi}^{\mathrm{T}}\Delta\boldsymbol{u} - \left(\gamma_1\, k_1 - \mu^2\right) z_1^{\mathrm{T}} z_1 - k_2\left(z_2 - \boldsymbol{\xi}\right)^{\mathrm{T}}\left(z_2 - \boldsymbol{\xi}\right) \\ &\quad - \left(k_3 - \frac{\gamma_1^2}{4\mu^2}\right)\boldsymbol{\xi}^{\mathrm{T}}\boldsymbol{\xi} - \left(\mu z_1 - \frac{\gamma_1}{2\mu}\boldsymbol{\xi}\right)^{\mathrm{T}}\left(\mu z_1 - \frac{\gamma_1}{2\mu}\boldsymbol{\xi}\right) \\ &\leq -2\rho V_2 + \sqrt{2}\varphi\sqrt{V_2},\end{aligned}$$

where $\mu > 0$, $\gamma_1\, k_1 - \mu^2 > 0$ and $k_3 - \gamma_1^2/\left(4\mu^2\right) > 0$. Additionally, ρ is given by

$$\rho = \min\left\{\gamma_1\, k_1 - \mu^2, k_2, k_3 - \frac{\gamma_1^2}{4\mu^2}\right\} > 0.$$

Employing the comparison principle again [31], we have

$$\sqrt{V_2\left(t\right)} \leq \left[\sqrt{V_2\left(0\right)} - \frac{\varphi}{\sqrt{2}\rho}\right]\exp\left(-2\rho t\right) + \frac{\varphi}{\sqrt{2}\rho}. \tag{43}$$

Therefore, the states of the closed-loop system composed of (38), (39), (41), and (42) are uniformly ultimately bounded. Invoking the definition in (32), one has

$$\limsup_{t\to\infty} \parallel \boldsymbol{r} - \boldsymbol{r}_d \parallel_2 \leq \frac{\varphi}{\sqrt{2}\gamma_1\rho}.$$

To get the commanded acceleration $\boldsymbol{a}_c$, we take the time derivative of (37) to yield

$$\begin{aligned}\dot{z}_2 = &-2\boldsymbol{\omega}\times\boldsymbol{v} - \boldsymbol{\omega}\times\left(\boldsymbol{\omega}\times\boldsymbol{r}\right) + \boldsymbol{g} + \boldsymbol{u} \\ &+ \Delta\boldsymbol{u} + \boldsymbol{d} + k_1\dot{z}_1 - \ddot{\boldsymbol{r}}_d.\end{aligned} \tag{44}$$

Equation (41) substituting for $\dot{z}_2$ in (44), the control input $\boldsymbol{u}$ can be derived as

$$\begin{aligned}\boldsymbol{u} = &-\gamma_1 z_1 - k_1\dot{z}_1 - k_2\left(z_2 - \boldsymbol{\xi}\right) \\ &- k_3\boldsymbol{\xi} + 2\boldsymbol{\omega}\times\boldsymbol{v} + \boldsymbol{\omega}\times\left(\boldsymbol{\omega}\times\boldsymbol{r}\right) - \boldsymbol{g} - \boldsymbol{d} + \ddot{\boldsymbol{r}}_d,\end{aligned} \tag{45}$$
$$\dot{\boldsymbol{\xi}} = -k_3\boldsymbol{\xi} + \Delta\boldsymbol{u}. \tag{46}$$

Remark 2: It is assumed that the saturation error $\Delta\boldsymbol{u}$ is bounded, but nevertheless the upper bound of $\Delta\boldsymbol{u}$ is unnecessary to be known. When the controller is not saturated (i.e. $\varphi = 0$), the control errors will converge to zero asymptotically according to (43).

B. SATURATED BACKSTEPPING CONTROLLER WITHOUT VELOCITY FEEDBACK

With application of the proposed ESO in Sec. II, the velocity $\boldsymbol{v}$ and the unknown disturbance $\boldsymbol{d}$ can be estimated from the measurements of the position vector simultaneously. Replacing $\boldsymbol{v}$ and $\boldsymbol{d}$ in (45) with the estimates $\hat{\boldsymbol{v}}$ and $\hat{\boldsymbol{d}}$ leads to

$$\begin{aligned}\boldsymbol{u}_r = &-\gamma_1 z_1 - k_1\hat{\dot{z}}_1 - k_2\left(\hat{z}_2 - \boldsymbol{\xi}\right) - k_3\boldsymbol{\xi} \\ &+ 2\boldsymbol{\omega}\times\hat{\boldsymbol{v}} + \boldsymbol{\omega}\times\left(\boldsymbol{\omega}\times\boldsymbol{r}\right) - \boldsymbol{g} - \hat{\boldsymbol{d}} + \ddot{\boldsymbol{r}}_d,\end{aligned} \tag{47}$$

where

$$\hat{\dot{z}}_1 = \gamma_1\left(\hat{\boldsymbol{v}} - \dot{\boldsymbol{r}}_d\right), \tag{48}$$
$$\hat{z}_2 = \hat{\boldsymbol{v}} + k_1 z_1 - \dot{\boldsymbol{r}}_d, \tag{49}$$
$$\dot{\boldsymbol{\xi}} = -k_3\boldsymbol{\xi} + \Delta\boldsymbol{u}. \tag{50}$$

To establish the stability of the system in (1) and (1) with the control input given by (47)-(50), $\hat{\boldsymbol{v}}$ and $\hat{\boldsymbol{d}}$ estimated by the ESO in (3)-(8), the following Lyapunov function candidate is considered:

$$V = V_2 + V_\vartheta.$$

Define vector

$$\boldsymbol{\eta} = \left[z_1^{\mathrm{T}},\ \left(z_2 - \boldsymbol{\xi}\right)^{\mathrm{T}},\ \boldsymbol{\xi}^{\mathrm{T}},\ \sqrt{2}\left(M\vartheta\right)^{\mathrm{T}}\right]^{\mathrm{T}},$$

and then V can be rewritten as

$$V = \frac{1}{2}\boldsymbol{\eta}^{\mathrm{T}}\boldsymbol{\eta}, \tag{51}$$

where $M^{\mathrm{T}}M = P$. Differentiating V with respect to time results in

$$\dot{V} = z_1^{\mathrm{T}}\left(-k_1\gamma_1 z_1 + \gamma_1 z_2\right) + \left(z_2 - \boldsymbol{\xi}\right)^{\mathrm{T}}\left[-2\boldsymbol{\omega}\times\boldsymbol{v}\right.$$

$$- \boldsymbol{\omega} \times (\boldsymbol{\omega} \times \boldsymbol{r}) + \boldsymbol{g} + \boldsymbol{u} + \Delta\boldsymbol{u} + \boldsymbol{d} + k_1 \dot{z}_1 - \ddot{\boldsymbol{r}}_d - (-k_3\boldsymbol{\xi} + \Delta\boldsymbol{u})] + \boldsymbol{\xi}^{\mathrm{T}} (-k_3\boldsymbol{\xi} + \Delta\boldsymbol{u}) + \boldsymbol{\vartheta}^{\mathrm{T}} P\dot{\boldsymbol{\vartheta}} + \dot{\boldsymbol{\vartheta}}^{\mathrm{T}} P\boldsymbol{\vartheta}. \quad (52)$$

Recall (33), (37), (48), and (49), and the following relationship can be achieved:

$$\hat{\dot{z}}_1 = \gamma_1 \left(\hat{\boldsymbol{v}} - \dot{\boldsymbol{r}}_d + \boldsymbol{v} - \boldsymbol{v}\right) = \dot{z}_1 - \gamma_1 \tilde{\boldsymbol{v}}, \quad (53)$$

$$\hat{z}_2 = \hat{\boldsymbol{v}} + k_1 z_1 - \dot{\boldsymbol{r}}_d + \boldsymbol{v} - \boldsymbol{v} = z_2 - \tilde{\boldsymbol{v}}. \quad (54)$$

Substituting (53) and (54) into (47) yields

$$\boldsymbol{u}_r = -\gamma_1 z_1 - k_1 (\dot{z}_1 - \gamma_1 \tilde{\boldsymbol{v}}) - k_2 (z_2 - \tilde{\boldsymbol{v}} - \boldsymbol{\xi}) - k_3 \boldsymbol{\xi} + 2\boldsymbol{\omega} \times \hat{\boldsymbol{v}} + \boldsymbol{\omega} \times (\boldsymbol{\omega} \times \boldsymbol{r}) - \boldsymbol{g} - \hat{\boldsymbol{d}} + \ddot{\boldsymbol{r}}_d. \quad (55)$$

Control variable $\boldsymbol{u}$ in (52) replaced with the right-hand side of (55), the derivative of the Lyapunov function can be further written as

$$\begin{aligned}
\dot{V} &= -k_1\gamma_1 z_1^{\mathrm{T}} z_1 + \gamma_1 z_1^{\mathrm{T}} z_2 + (z_2 - \boldsymbol{\xi})^{\mathrm{T}} \Big[-2\boldsymbol{\omega} \times \tilde{\boldsymbol{v}} - \gamma_1 z_1 \\
&\quad + k_1\gamma_1 \tilde{\boldsymbol{v}} - k_2 (z_2 - \boldsymbol{\xi}) + k_2 \tilde{\boldsymbol{v}} + \tilde{\boldsymbol{d}}\Big] + \boldsymbol{\xi}^{\mathrm{T}} [-k_3\boldsymbol{\xi} + \Delta\boldsymbol{u}] \\
&\quad + \boldsymbol{\vartheta}^{\mathrm{T}} P\dot{\boldsymbol{\vartheta}} + \dot{\boldsymbol{\vartheta}}^{\mathrm{T}} P\boldsymbol{\vartheta} \\
&\le -k_1\gamma_1 \|z_1\|_2^2 - k_2 \|z_2 - \boldsymbol{\xi}\|_2^2 - k_3 \|\boldsymbol{\xi}\|_2^2 \\
&\quad - \left\|\alpha_1 z_1 - \frac{\gamma_1}{2\alpha_1}\boldsymbol{\xi}\right\|_2^2 - \left\|\alpha_3 (z_2 - \boldsymbol{\xi}) - \frac{1}{2\alpha_3}\tilde{\boldsymbol{d}}\right\|_2^2 \\
&\quad - \left\|\alpha_2 (z_2 - \boldsymbol{\xi}) - \frac{1}{2\alpha_2}\left(k_1\gamma_1 I_3 + k_2 I_3 - 2\boldsymbol{\omega}^{\times}\right)\tilde{\boldsymbol{v}}\right\|_2^2 \\
&\quad + \alpha_1^2 \|z_1\|_2^2 + \frac{\gamma_1^2}{4\alpha_1^2} \|\boldsymbol{\xi}\|_2^2 + \alpha_2^2 \|z_2 - \boldsymbol{\xi}\|_2^2 \\
&\quad + \frac{1}{4\alpha_2^2} \left\|\left(k_1\gamma_1 I_3 + k_2 I_3 - 2\boldsymbol{\omega}^{\times}\right)\tilde{\boldsymbol{v}}\right\|_2^2 + \alpha_3^2 \|z_2 - \boldsymbol{\xi}\|_2^2 \\
&\quad + \frac{1}{4\alpha_3^2} \left\|\tilde{\boldsymbol{d}}\right\|_2^2 + \boldsymbol{\xi}^{\mathrm{T}} \Delta\boldsymbol{u} - \varepsilon^{-5}\lambda_{\min}(Q) \|\boldsymbol{\zeta}\|_2^2 \\
&\quad - \varepsilon^{-3}\lambda_{\min}(Q) \|\tilde{\boldsymbol{v}}\|_2^2 - \varepsilon^{-1}\lambda_{\min}(Q) \left\|\tilde{\boldsymbol{d}}\right\|_2^2 \\
&\quad + 2\lambda_{\max}(P)\, \psi \|\boldsymbol{\vartheta}\|_2 .
\end{aligned}$$

According to the property of norms, one has

$$\left\|\left(k_1 I_3 + k_2 I_3 - 2\boldsymbol{\omega}^{\times}\right)\tilde{\boldsymbol{v}}\right\|_2 \le \left\|k_1 I_3 + k_2 I_3 - 2\boldsymbol{\omega}^{\times}\right\|_{\mathrm{F}} \|\tilde{\boldsymbol{v}}\|_2 .$$

Thus,

$$\begin{aligned}
\dot{V} &\le -\left(k_1\gamma_1 - \alpha_1^2\right)\|z_1\|_2^2 - \left(k_2 - \alpha_2^2 - \alpha_3^2\right)\|z_2 - \boldsymbol{\xi}\|_2^2 \\
&\quad - \left(k_3 - \frac{\gamma_1^2}{4\alpha_1^2}\right)\|\boldsymbol{\xi}\|_2^2 - \left\|\alpha_1 z_1 - \frac{\gamma_1}{2\alpha_1}\boldsymbol{\xi}\right\|_2^2 \\
&\quad - \left\|\alpha_2 (z_2 - \boldsymbol{\xi}) - \frac{1}{2\alpha_2}\left(k_1\gamma_1 I_3 + k_2 I_3 - 2\boldsymbol{\omega}^{\times}\right)\tilde{\boldsymbol{v}}\right\|_2^2 \\
&\quad - \left\|\alpha_3 (z_2 - \boldsymbol{\xi}) + \frac{1}{2\alpha_3}\tilde{\boldsymbol{d}}\right\|_2^2 - \varepsilon^{-1}\lambda_{\min}(Q) \|\boldsymbol{\vartheta}_1\|_2^2 \\
&\quad - \left[\varepsilon^{-1}\lambda_{\min}(Q) - \frac{\varepsilon^2}{4\alpha_2^2}\left\|k_1\gamma_1 I_3 + k_2 I_3 - 2\boldsymbol{\omega}^{\times}\right\|_{\mathrm{F}}^2\right] \\
&\quad \times \|\boldsymbol{\vartheta}_2\|_2^2 - \left[\varepsilon^{-1}\lambda_{\min}(Q) - \frac{1}{4\alpha_3^2}\right]\|\boldsymbol{\vartheta}_3\|_2^2 \\
&\quad + 2\lambda_{\max}(P)\, \psi \|\boldsymbol{\vartheta}\|_2 + \varphi \|\boldsymbol{\xi}\|_2 ,
\end{aligned}$$

where $\alpha_1, \alpha_2, \alpha_3, \alpha_4 \in \mathbb{R}^+$, and the following inequalities are satisfied:

$$k_1\gamma_1 - \alpha_1^2 > 0, \quad k_2 - \alpha_2^2 - \alpha_3^2 > 0, \; k_3 - \frac{\gamma_1^2}{4\alpha_1^2} > 0,$$

$$\varepsilon^{-1}\lambda_{\min}(Q) - \frac{\varepsilon^2}{4\alpha_2^2}\left\|k_1\gamma_1 I_3 + k_2 I_3 - 2\boldsymbol{\omega}^{\times}\right\|_{\mathrm{F}}^2 > 0,$$

$$\varepsilon^{-1}\lambda_{\min}(Q) - \frac{1}{4\alpha_3^2} > 0.$$

Consequently, we have

$$\begin{aligned}
\dot{V} &\le -a_1 \left(\|z_1\|_2^2 + \|z_2 - \boldsymbol{\xi}\|_2^2 + \|\boldsymbol{\xi}\|_2^2\right) \\
&\quad - a_2 \left(\|\boldsymbol{\vartheta}_1\|_2^2 + \|\boldsymbol{\vartheta}_2\|_2^2 + \|\boldsymbol{\vartheta}_3\|_2^2\right) + a_3 \|\boldsymbol{\xi}\|_2 \\
&\le -2a_1 V_2 - \frac{a_2}{\lambda_{\max}(P)} V_{\vartheta} + a_3 \|\boldsymbol{\eta}\|_2 , \quad (56)
\end{aligned}$$

where

$$a_1 = \min\left\{\gamma_1 k_1 - \alpha_1^2,\; k_2 - \alpha_2^2 - \alpha_3^2,\; k_3 - \frac{\gamma_1^2}{4\alpha_1^2}\right\}, \quad (57)$$

$$a_2 = \min\left\{\frac{\lambda_{\min}(Q)}{\varepsilon} - \frac{\varepsilon^2 \left\|k_1\gamma_1 I_3 + k_2 I_3 - 2\boldsymbol{\omega}^{\times}\right\|_{\mathrm{F}}^2}{4\alpha_2^2},\; \frac{\lambda_{\min}(Q)}{\varepsilon} - \frac{1}{4\alpha_3^2}\right\}, \quad (58)$$

$$a_3 = \max\{2\lambda_{\max}(P)\, \psi,\; \varphi\}. \quad (59)$$

Invoking (51), one can write (56) as

$$\dot{V} \le -2c_1 V + \sqrt{2}c_2\sqrt{V}, \quad (60)$$

where

$$c_1 = \min\left\{a_1,\; \frac{a_2}{2\lambda_{\max}(P)}\right\}, \quad c_2 = a_3.$$

Application of the comparison principle to (60) yields

$$\sqrt{V(t)} \le \left[\sqrt{V(0)} - \frac{c_2}{\sqrt{2}c_1}\right]\exp(-2\, c_1\, t) + \frac{c_2}{\sqrt{2}c_1}.$$

Thus,

$$\limsup_{t\to\infty} \|\boldsymbol{\eta}\|_2 = \limsup_{t\to\infty} \sqrt{2\, V(t)} = \frac{c_2}{c_1}.$$

Therefore, $\boldsymbol{\eta}$ is uniformly ultimately bounded with the ultimate bound c_2/c_1.

Recall the definition of $\boldsymbol{\eta}$ and (32), and it is readily to get

$$\limsup_{t\to\infty} \|\boldsymbol{r} - \boldsymbol{r}_d\|_2 \le \frac{c_2}{c_1\gamma_1}.$$

It is evident that the proposed controller uniformly ultimately bounds the hovering error on the neighborhood of zero as $t \to \infty$ with properly selected parameters. It should be noted that $\boldsymbol{r}_d$ can be either constant or time-varying, and therefore the

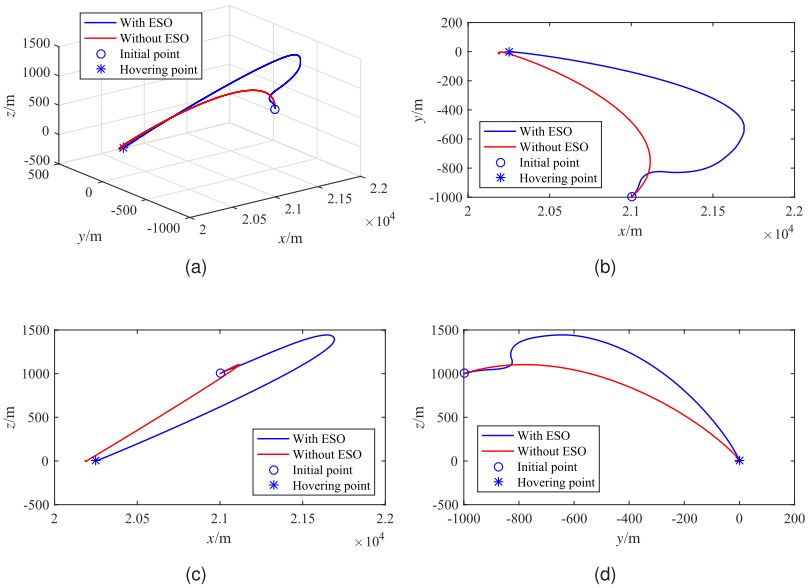

FIGURE 3. Controlled trajectories in the body-fixed hovering scenario: (a) three-dimensional trajectories, (b) trajectories projected onto the *x*-*y* plane, (c) trajectories projected onto the *x*-*z* plane, (d) trajectories projected onto the *y*-*z* plane.

controller is suitable for both body-fixed hovering and inertial hovering.

Remark 3: For the same controllers, the parameters $\gamma_1, k_1, k_2, \alpha_1, \alpha_2, \alpha_3, \varepsilon$, etc. are not unique. Different combinations of them could lead to different estimates of the upper bounds of the final control errors, hence the best estimates of the upper bounds should be the minimum ones among the estimates.

Remark 4: From the analysis of the ESO, we have known that reducing ε amplifies the influence of measurement errors. Besides, a too small ε may also result in unacceptable upper bounds of the final control errors, just as is indicated by (58).

V. NUMERICAL SIMULATIONS

In this section, numerical simulations are carried out to demonstrate the effectiveness of the proposed controller. The asteroid 433 Eros is taken as the target asteroid and its polyhedron shape model is shown in Fig. 2. The gravitational parameter μ of 433 Eros is $4.46275472004 \times 10^5$ m^3/s^2, with the bulk density of 2.67 g/cm^3, the rotation period of 5.27 hours [1]. To demonstrate the effectiveness of the proposed controller, both body-fixed hovering and inertial hovering are tested.

It is assumed that the maximum magnitude of the commanded acceleration generated by the thrusters in each direction is 1×10^{-2} m/s^2. To assess the influence of the measurement noise of $\boldsymbol{r}$ on the ESO, the true position vector is corrupted with Gaussian noise with 0 m mean and 0.1 m standard deviation. The uncertainties and the disturbances [15], [18] are mimicked by

$$\boldsymbol{d} = \begin{bmatrix} 1.5\sin(\omega t) + 0.15\sin\left(10\omega t + \frac{\pi}{2}\right) \\ 2.1\sin\left(\omega t + \frac{\pi}{4}\right) + 0.21\sin\left(10\omega t + \frac{\pi}{4}\right) \\ 1.3\sin\left(\omega t + \frac{\pi}{2}\right) + 0.13\sin(10\omega t) \end{bmatrix} \times 10^{-5}\text{m/s}^2 + 0.1 \times \boldsymbol{g}(\boldsymbol{r}). \quad (61)$$

The first part of the right-hand side of (61) represents the disturbances caused by solar radiation pressure and the gravitational effects of other celestial bodies. Because the asteroid rotates around its axis of the maximum inertial moment, the disturbances include periodical components with the same frequency as the rotational frequency. The higher frequency components appear in (59) to consider other periodical disturbances. Evidently, the second part illustrates a gravitational uncertainty that is equal to 10% of the local gravitational acceleration. Both in the real world and according to the polyhedron model, the asteroid gravitational acceleration $\boldsymbol{g}(\boldsymbol{r})$ and its change rate $\dot{\boldsymbol{g}}(\boldsymbol{r})$ are bounded, hence $\boldsymbol{d}$ and $\dot{\boldsymbol{d}}$ both bounded according to (61).

A. BODY-FIXED HOVERING

The body-fixed hovering scenario is tested first. The initial position and initial velocity of the spacecraft are given by $\boldsymbol{r}_0 = [21, -1, 1]^{\mathrm{T}} \times 10^3$ m and $\boldsymbol{v}_0 = [1, 1, 1]^{\mathrm{T}}$ m/s, respectively. The desired hovering point is set at $\boldsymbol{r}_d = [20.25, 0, 0]^{\mathrm{T}} \times 10^3$ m. Evidently, the desired velocity is $\boldsymbol{v}_d = [0, 0, 0]^{\mathrm{T}}$ m/s for body-fixed hovering. Before proceeding to the simulation, the parameters of the controller are given in Table 1.

For the sake of verifying the effectiveness of the ESO, both of the body-fixed hovering trajectories with and without the

TABLE 1. Parameters of the controller for body-fixed hovering.

Parameter	Value
γ_1	1.5×10^{-3}
k_1	0.1
k_2	3.0×10^{-3}
k_3	1.0×10^{-2}
ε	1.0
h_1	5.0×10^{-2}
h_2	1.1×10^{-3}
h_3	1.0×10^{-5}

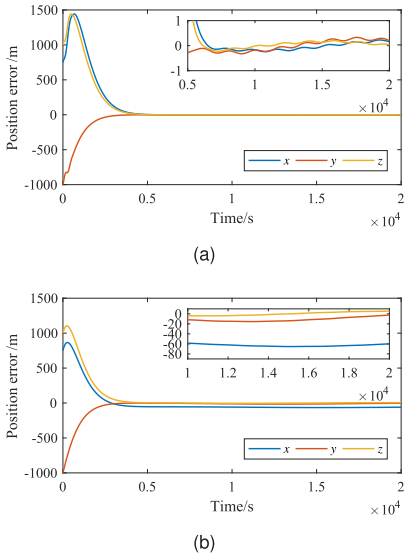

FIGURE 4. Position errors of the body-fixed hovering: (a) controller with ESO, (b) controller without ESO.

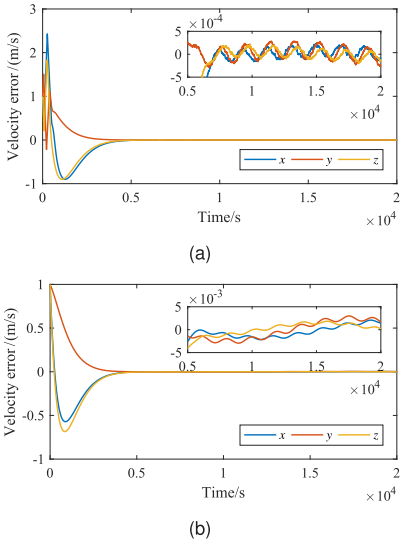

FIGURE 5. Velocity errors of the body-fixed hovering: (a) controller with ESO, (b) controller without ESO.

ESO are illustrated in the body-fixed frame $o-xyz$ in Fig. 3. It shows that the trajectory with the ESO deviates from the hovering point in the initial phase, then makes great efforts to correct the mistake to approach the hovering point, and finally maintains its terminal position in the neighborhood of the hovering point. The abnormal behavior of the trajectory is resulted from the fact that the outputs of the ESO have not converged to the neighborhood of the real values in the initial phase. Although, it seems that the controlled trajectory with the ESO is not so elegant as the one without the ESO, the final hovering accuracy of the former is much higher than that of the latter as revealed by Fig. 4. From the figure, we can see that the final position errors of the controller equipped with the ESO are smaller than 1 m. On the contrary, the position errors of the controller without the ESO are in the order of 10 m. The corresponding velocity errors are plotted in Fig. 5. Unsurprisingly, the controller with the ESO outperforms the one without the ESO, as the figure indicates.

Fig. 6 gives the profiles of the commanded acceleration of the proposed controller. It is evident that the control input oscillates in the initial phase, and then shrinks to the neighborhood of the constant values to cancel out the local gravity and reject the disturbances. The oscillations of the controller mainly result from the ESO, which can be readily inferred from the profiles of the ESO's outputs.

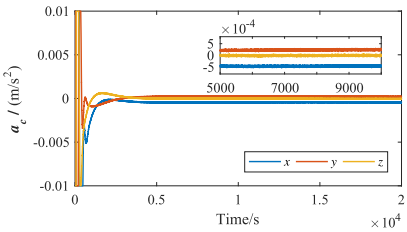

FIGURE 6. Commanded acceleration of the body-fixed hovering.

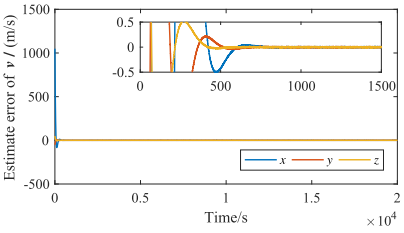

FIGURE 7. Estimate error of v in the body-fixed hovering scenario.

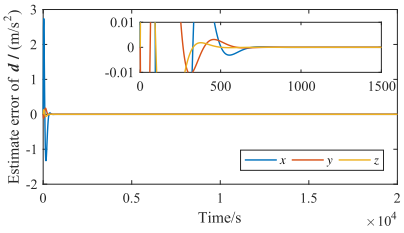

FIGURE 8. Estimate error of d in the body-fixed hovering scenario.

B. INERTIAL HOVERING

Fig. 7 and Fig. 8 report the estimate errors of $\boldsymbol{v}$ and $\boldsymbol{d}$ respectively. All of the estimate errors converge to the neighborhood of zero after a few transient oscillations. Actually, reducing the ESO parameter ε can attenuate the oscillation, but the measurement noise of $\boldsymbol{r}$, meanwhile, can be amplified to corrupt the estimation outputs. Therefore, the profiles shown in the figures are the results of balancing the transient performance and the accuracy of the outputs. In the practice, the measurements of $\boldsymbol{r}$ are fed to a filter first to refine the input signals before they are applied to the controller, which can greatly reduce the adverse influence of the measurement noise. From the figures, we can seen that the estimate errors are in the neighborhood of zero, and the accuracy is adequate

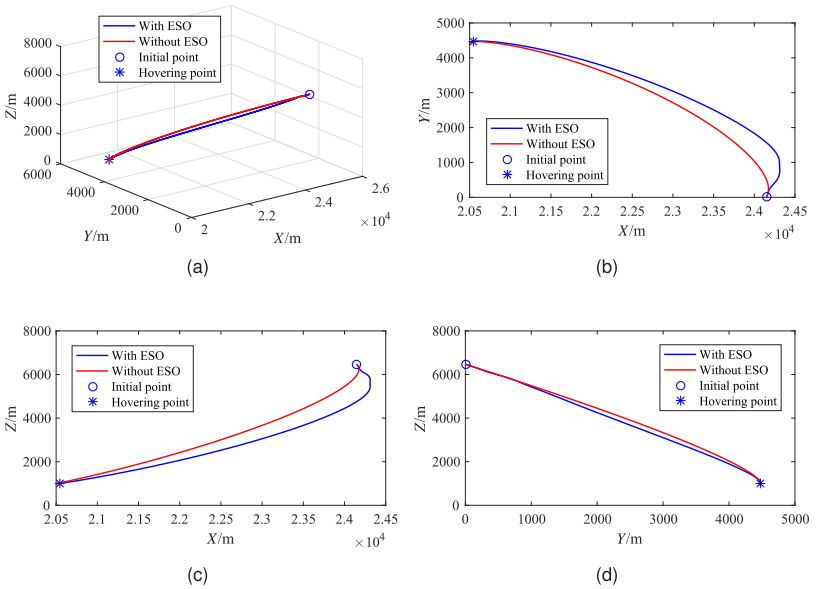

FIGURE 9. Controlled trajectories in the inertial hovering scenario: (a) three-dimensional trajectories, (b) trajectories projected onto the *X*-*Y* plane, (c) trajectories projected onto the *X*-*Z* plane, (d) trajectories projected onto the *Y*-*Z* plane.

TABLE 2. Parameters of the controller for inertial hovering.

Parameter	Value
γ_1	1.8×10^{-3}
k_1	0.1
k_2	3.6×10^{-3}
k_3	1.0×10^{-2}
ε	0.5
h_1	0.1
h_2	4.0×10^{-3}
h_3	8.0×10^{-5}

for the hovering control, which can be confirmed by the position error profiles in Fig. 4 and the velocity error profiles in Fig. 5. For inertial hovering, the initial position and initial velocity of the spacecraft are identified in the inertial frame by the vectors

$$\boldsymbol{r}_0^I = r_0^I \times \left[\cos\left(\frac{\pi}{12}\right),\ 0,\ \sin\left(\frac{\pi}{12}\right)\right]^{\mathrm{T}},$$
$$\boldsymbol{v}_0^I = \sqrt{\frac{\mu}{r_0^I}} \times \begin{bmatrix} \sin\left(\frac{\pi}{4}\right)\sin\left(\frac{\pi}{12}\right) \\ \cos\left(\frac{\pi}{4}\right) \\ -\sin\left(\frac{\pi}{4}\right)\cos\left(\frac{\pi}{12}\right) \end{bmatrix},$$

where $r_0^I = 2.5 \times 10^4$ m. The desired hovering location in the inertial coordinate frame $O - XYZ$ is set to

$$\boldsymbol{R}_d^I = T^{-1}\left(\frac{\pi}{12}\right) \times [2.1,\ -0.1,\ 0.1]^{\mathrm{T}} \times 10^4 \text{ m},$$

and the desired velocity in the inertial frame should be zero, that is $\boldsymbol{V}_d^I = 0_{3\times 1}$. Inertial hovering is more demanding than body-fixed hovering because the desired position $\boldsymbol{r}_d$ is not constant any more in the body-fixed coordinate frame. Thereby, the gravity at the hovering point also varies with the rotation of the asteroid beneath the spacecraft. Certainly,

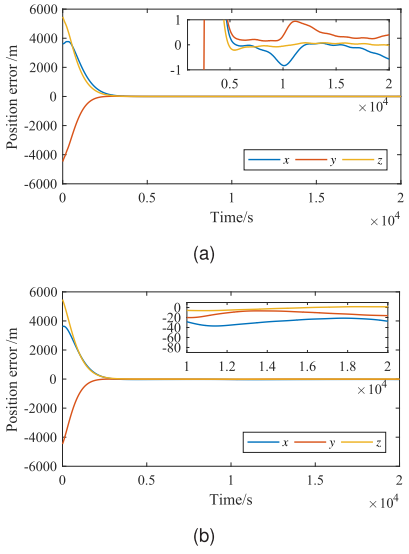

FIGURE 10. Position errors of the inertial hovering: (a) controller with ESO; (b) controller without ESO.

the parameters of the controller and the ESO have to be re-tuned to cope with the challenging. The parameters for inertial hovering are listed in Table 2.

Fig. 9 shows the controlled trajectories of the inertial hovering. It can be seen that both of the trajectories resulted from the controllers with and without the ESO extend smoothly and vary reasonably. Similar to the body-fixed hovering, because the outputs of the ESO have not converged to the neighborhood of the real values in the initial phase, the trajectory resulted from the controller with the ESO dose not coincide with the trajectory driven by the velocity-feedback controller.

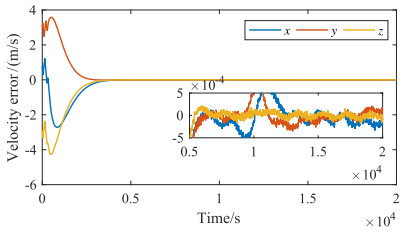

(a)

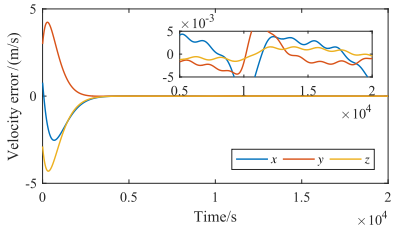

(b)

FIGURE 11. Velocity errors of the inertial hovering: (a) controller with ESO; (b) controller without ESO.

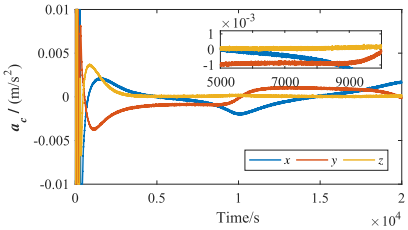

FIGURE 12. Commanded acceleration of the body-fixed hovering.

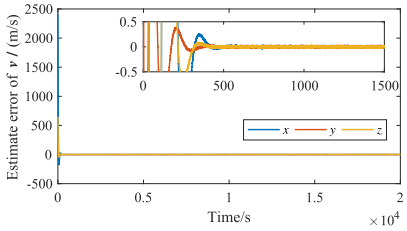

FIGURE 13. Estimate error of v in the inertial hovering scenario.

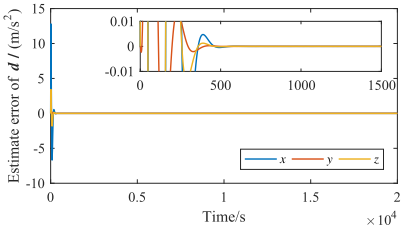

FIGURE 14. Estimate error of d in the inertial hovering scenario.

After the transient process of the ESO, the two trajectories become similar to each other. However, the final accuracy of them is quite different just as what happened in the body-fixed hovering. The position error profiles and the velocity error profiles are illustrated in Fig. 10 and Fig. 11, respectively. Even in the inertial hovering, the proposed controller can still steer the spacecraft to the desired point and maintain a hovering condition with position accuracy of 1 m and a residual velocity below 5.0×10^{-4} m/s. On the contrary, however, the controller without the ESO has much lower accuracy on both position and velocity.

The commanded acceleration is reported in Fig. 12. The control acceleration in the body-fixed hovering tends to converge to constants, whereas the control acceleration at the inertial hovering point varies slowly with the desired position moving in the body-fixed coordinate frame. Another notable difference is that the influence of the measurement noise on the control acceleration is stronger in the inertial hovering because of the larger gains of the ESO.

Fig. 13 and Fig. 14 give the profiles of the estimate errors of $\boldsymbol{v}$ and $\boldsymbol{d}$ in the inertial hovering scenario, respectively. As can be seen, the estimate accuracy tends to deteriorate a little under the influence of the measurement noise. From (7) and (8), it is easy to find that the measurement noise is injected into $\hat{\boldsymbol{v}}$ directly, thereby $\hat{\boldsymbol{v}}$ prone to be contaminated by the noise. However, for the estimated disturbance $\hat{\boldsymbol{d}}$, an integration operation is applied to the noise before it enters $\hat{\boldsymbol{d}}$. Hence, $\hat{\boldsymbol{v}}$ suffers the measurement noise more greatly than $\hat{\boldsymbol{d}}$, as the figures show. Nevertheless, the estimated values are still precise enough to implement accurate inertial hovering.

VI. CONCLUSION

This paper presents a backstepping control scheme for both body-fixed hovering and inertial hovering over an asteroid without velocity measurement, which can reject the large disturbances in the vicinity of asteroids and cope with the control input saturation caused by the limited control authority of the spacecraft in asteroid exploration missions. To attain the control goal, a novel ESO is designed first to estimate the velocity and the lumped disturbance simultaneously. With the assumption that the change rate of the total disturbance is bounded, the estimate errors of the ESO is proved to be uniformly ultimately bounded. In order to deal with the control input saturation, a backstepping controller is combined with an auxiliary system to guarantee the stability of the closed-loop system in the presence of control input saturation. Finally, the velocity in the basic controller is replaced with the estimate and the lumped disturbance is compensated for by the estimated disturbance, which completes the disturbance rejection saturated controller without velocity measurement. The stability of the whole closed-loop system is analyzed via Lyapunov theory, which shows that the states of the system is uniformly ultimately bounded.

Numerical simulations demonstrate the effectiveness of the proposed method. Through the comparison between the controller with and without the ESO, it is easy to find that the ESO plays an key role in improving the hovering accuracy. In the extensively investigated sliding mode control,

the good performance relies on the high gain (upper bound of the disturbance) switching term. Not only is the high gain unnecessary, but also the supremum of the disturbance is hard to be obtained a priori for asteroid exploration missions. The proposed control scheme neither relies on velocity measurements nor requires a priori knowledge about disturbances, and therefore is preferable to asteroid hovering.

REFERENCES

[1] B. Zhang, Y. Cai, and F. Li, "Adaptive double-saturated control for hovering over an asteroid," *Adv. Space Res.*, vol. 63, no. 7, pp. 2035–2051, Apr. 2019.

[2] H. Ikeda, T. Kominato, M. Matsuoka, T. Ohnishi, and M. Yoshikawa, "Orbit determination of Hayabusa during close proximity phase," *Trans. JSASS Space Tech. Jpn.*, vol. 7, no. 26, pp. 119–124, 2009.

[3] S. Sawai and D. J. Scheeres, "Control of hovering spacecraft using altimetry," *J. Guid. Control Dyn.*, vol. 25, no. 4, pp. 786–795, Jul./Aug. 2002.

[4] S. B. Broschart and D. J. Scheeres, "Control of hovering spacecraft near small bodies: Application to Asteroid 25143 Itokawa," *J. Guid. Control Dyn.*, vol. 28, no. 2, pp. 343–354, Mar./Apr. 2005.

[5] B. S. Broschart and D. J. Scheeres, "Boundedness of spacecraft hovering under dead-band control in time-invariant systems," *J. Guid. Control Dyn.*, vol. 30, no. 2, pp. 601–610, Mar./Apr. 2007.

[6] B. Gaudet and R. Furfaro, "Robust spacecraft hovering near small bodies in environments with unknown dynamics using reinforcement learning," in *Proc. AIAA/AAS Astrodynamics Spec. Conf.*, AIAA, Aug. 2012, p. 5027.

[7] M. Nazari, R. Wauson, T. Critz, E. A. Butcher, and D. J. Scheeres, "Observer-based body-frame hovering control over a tumbling asteroid," *Acta Astronaut.*, vol. 102, pp. 124–139, Sep. 2014.

[8] R. Furfaro, "Hovering in asteroid dynamical environments using higher-order sliding control," *J. Guid. Control Dyn.*, vol. 38, no. 2, pp. 263–279, Feb. 2015.

[9] X.-Y. Zeng, F.-H. Jiang, and J.-F. Li, "Asteroid body-fixed hovering using nonideal solar sails," *Res. Astron. Astrophys.*, vol. 15, no. 4, pp. 597–607, 2015.

[10] X. Zeng, S. Gong, J. Li, and K. T. Alfriend, "Solar sail body-fixed hovering over elongated asteroids," *J. Guid. Control Dyn.*, vol. 39, no. 3, pp. 1223–1231, Jun. 2016.

[11] D. Lee and G. Vukovich, "Adaptive sliding mode control for spacecraft body-fixed hovering in the proximity of an asteroid," *Aerosp. Sci. Technol.*, vol. 46, pp. 471–483, Oct./Nov. 2015.

[12] D. Lee, A. K. Sanyal, E. A. Butcher, and D. J. Scheere, "Finite-time control for spacecraft body-fixed hovering over an asteroid," *IEEE Trans. Aerosp. Electron. Syst.*, vol. 51, no. 1, pp. 506–519, Jan. 2015.

[13] D. Lee and G. Vukovich, "Adaptive finite-time control for spacecraft hovering over an asteroid," *IEEE Trans. Aerosp. Electron. Syst.*, vol. 52, no. 3, pp. 1183–1196, Jun. 2016.

[14] Y. Wang and S. Xu, "Body-fixed orbit-attitude hovering control over an asteroid using non-canonical Hamiltonian structure," *Acta Astronautica*, vol. 117, pp. 450–468, Dec. 2015.

[15] X. Liu, P. Zhang, K. Liu, and Y. Li, "Compensator-based 6-DOF control for probe asteroid-orbital-frame hovering with actuator limitations," *Adv. Space Res.*, vol. 57, no. 9, pp. 1914–1927, May 2016.

[16] H. Gui and A. H. J. D. Ruiter, "Control of asteroid-hovering spacecraft with disturbance rejection using position-only measurements," *J. Guid. Control Dyn.*, vol. 40, no. 10, pp. 2401–2416, Jun. 2017.

[17] H. Yang, X. Bai, and H. Baoyin, "Finite-time control for asteroid hovering and landing via terminal sliding-mode guidance," *Acta Astronaut.*, vol. 132, pp. 78–89, Mar. 2017.

[18] B. Zhang and Y. Cai, "Immersion and invariance based adaptive backstepping control for body-fixed hovering over an asteroid," *IEEE Access*, vol. 7, no. 1, pp. 34850–34861, Apr. 2019.

[19] L. Sun and Z. Zheng, "Disturbance-observer-based robust backstepping attitude stabilization of spacecraft under input saturation and measurement uncertainty," *IEEE Trans. Ind. Electron.*, vol. 64, no. 10, pp. 7994–8002, Oct. 2017.

[20] L. Sun, W. Huo, and Z. Jiao, "Disturbance-observer-based robust relative pose control for spacecraft rendezvous and proximity operations under input saturation," *IEEE Trans. Aerosp. Electron. Syst.*, vol. 54, no. 4, pp. 1605–1617, Aug. 2018.

[21] H. Yang, X. You, Y. Xia, and H. Li, "Adaptive control for attitude synchronisation of spacecraft formation via extended state observer," *IET Control Theory Appl.*, vol. 8, no. 18, pp. 2171–2185, Nov. 2014.

[22] S. Zarovy and M. Costello, "Extended state observer for helicopter mass and center-of-gravity estimation," *J. Aircr.*, vol. 52, no. 6, pp. 1939–1949, Nov./Dec. 2015.

[23] Q. Wang, M. Ran, and C. Dong, "Robust partial integrated guidance and control for missiles via extended state observer," *ISA Trans.*, vol. 65, pp. 27–36, Nov. 2016.

[24] B. Li, Q. Hu, and G. Ma, "Extended state observer based robust attitude control of spacecraft with input saturation," *Aerosp. Sci. Technol.*, vol. 50, pp. 173–182, Mar. 2016.

[25] L. Sun and Z. Zheng, "Adaptive relative pose control of spacecraft with model couplings and uncertainties," *Acta Astronaut.*, vol. 143, pp. 29–36, Feb. 2018.

[26] L. Sun, W. He, and C. Sun, "Adaptive fuzzy relative pose control of spacecraft during rendezvous and proximity maneuvers," *IEEE Trans. Fuzzy Syst.*, vol. 26, no. 6, pp. 3440–3451, Dec. 2018.

[27] J. Han, "From PID to active disturbance rejection control," *IEEE Trans. Ind. Electron.*, vol. 56, no. 3, pp. 900–906, Mar. 2009.

[28] D. K. Koria, J. P. Kolhe, and S. E. Talole, "Extended state observer based robust control of wing rock motion," *Aerosp. Sci. Technol.*, vol. 33, no. 1, pp. 107–117, Feb. 2014.

[29] X. Shao, J. Liu, and H. Wang, "Robust back-stepping output feedback trajectory tracking for quadrotors via extended state observer and sigmoid tracking differentiator," *Mech. Syst. Signal Proc.*, vol. 104, pp. 631–647, Mar. 2018.

[30] R. A. Werner and D. J. Scheeres, "Exterior gravitation of a polyhedron derived and compared with harmonic and mascon gravitation representations of asteroid 4769 Castalia," *Celest. Mech. Dyn. Astron.*, vol. 65, no. 3, pp. 313–344, Sep. 1997.

[31] H. K. Khalil, *Nonlinear System*, 3rd ed. Upper Saddle River, NJ, USA: Prentice Hall, 2002.

[32] B. Zhang, S. Tang, and B. Pan, "Robust trajectory tracking guidance for low L/D lunar return vehicles using command filtered backstepping approach," *J. Aerosp. Eng.*, vol. 31, no. 2, 2018, Art. no. 04017105.

BO ZHANG was born in Shaanxi, China, in 1988. He received the B.S. and Ph.D. degrees in aerospace engineering from the Department of Aerospace Design Engineering, Northwestern Polytechnical University, Xi'an, China, in 2010 and 2017, respectively. Since 2017, he has been a Postdoctoral Research Fellow with the School of Electronics and Information Engineering, Xi'an Jiaotong University. His current research interests include dynamics and control for asteroid explorations, spacecraft trajectory optimization, powered descent and landing, and reentry guidance.

YUANLI CAI was born in Guizhou, China, in 1963. He received the B.S. and Ph.D. degrees in aerospace engineering from Northwestern Polytechnical University, Xi'an, China, in 1984 and 1990, respectively. From 1993 to 1998, he was an Associate Professor with the School of Electronics and Information Engineering, Xi'an Jiaotong University, Xi'an. From 1998 to 1999, he was invited as a Senior Scholar with the Chinese Academy of Sciences. From 2003 to 2004, he visited the University of California at Riverside, Riverside, CA, USA. Since 1999, he has been a Professor with the School of Electronics and Information Engineering, Xi'an Jiaotong University. His research interests include guidance, control and dynamics of aircraft, intelligent information processing systems and technology, modeling and simulation of complex systems, and nonlinear theory and application. He is currently a Senior Member of the AIAA.